Tunable Collective Excitations in Epitaxial Perovskite Nickelates

Mengxia Sun,[1#] Xu He,[2#] Mingyao Chen,[1] Chi Sin Tang,[1,3,*] Xiongfang Liu,[1] Liang Dai,[1] Jishan Liu,[4] Zhigang Zeng,[1] Shuo Sun,[1] Mark B.H. Breese,[3,5] Chuanbing Cai,[1] Yingge Du,[6] Le Wang,[6,*] Andrew T. S. Wee,[5,7] Xinmao Yin[1,*]

[1]Shanghai Key Laboratory of High Temperature Superconductors, Department of Physics, Shanghai University, Shanghai 200444, China

[2]Theoretical Materials Physics, Q-MAT, CESAM, Université de Liège, B-4000 Liège, Belgium

[3]Singapore Synchrotron Light Source, National University of Singapore, Singapore 117603, Singapore

[4]State Key Laboratory of Functional Materials for Informatics, Shanghai Institute of Microsystem and Information Technology, Chinese Academy of Sciences, Shanghai 200050, China

[5]Department of Physics, Faculty of Science, National University of Singapore, Singapore 117542, Singapore

[6]Physical and Computational Sciences Directorate, Pacific Northwest National Laboratory, Richland, WA 99354, USA

[7]Centre for Advanced 2D Materials and Graphene Research, National University of Singapore, Singapore 117546, Singapore

*Corresponding author. Email: slscst@nus.edu.sg (C.S.T.); le.wang@pnnl.gov (L.W.); yinxinmao@shu.edu.cn (X.Y.)

# These authors contributed equally to this work.

Abstract

The formation of plasmons through the collective excitation of charge density has generated intense discussions, offering insights to fundamental sciences and potential applications. While the underlying physical principles have been well-established, the effects of multibody interactions and orbital hybridization on plasmonic dynamics remain understudied. In this work, we present the observation of conventional metallic and correlated plasmons in epitaxial $La_{1-x}Sr_xNiO_3$ (LSNO) films with varying Sr doping concentrations (x = 0, 0.125, 0.25), unveiling their intriguing evolution. Unlike samples at other doping concentrations, the x = 0.125 intermediate doping sample does not exhibit the correlated plasmons despite showing high optical conductivity. Through experimental investigation using spectroscopic ellipsometry and X-ray absorption spectroscopy, that is further supported by theoretical calculations, the O2*p*-Ni3*d* orbital hybridization for x = 0.125 is found to be significantly enhanced, alongside a considerable weakening of its effective interaction comprising long-range Coulomb and variable interaction, U^*. These factors account for the absence of correlated plasmons and the high optical conductivity observed in LSNO(0.125). Our findings highlight the significant impact of orbital hybridization on the electronic structures and the formation of quasiparticles in strongly correlated systems, opening new paths for plasmonic-based engineering research.

1. Introduction

The complex interactions between the lattice, charge, spin, and orbital degrees of freedom regulates the electronic and magnetic structures of strongly-correlated systems, resulting in intriguing physical phenomena including superconductivity, giant magnetoresistance effect, and metal-insulator transition[1-4]. The impact of multibody interactions and orbital hybridizations on the electronic properties remains a highly sought-after research domain in perovskite structure transition metal oxides[5-7]. Meanwhile, collective charge dynamics in the form of plasmon excitations are intimately linked to the electronic structure of strongly-correlated systems[8-10].

While conventional metallic plasmons have been observed in multiple strongly-correlated transition metal oxides[11-13], note that theoretical studies have revealed the interaction of both short- and long-range correlations in Mott insulating systems can produce unconventional plasmons known as 'correlated plasmons' which possess multiple photon energies[14]. These correlated plasmons have been experimentally observed in niobates, cuprates, and other topological materials[8, 10, 15], thereby emphasizing the role of charge-spin coupling in their formation. In strongly-correlated systems, while the orbital hybridization between the metallic $3d$ and oxygen $2p$ orbitals have been pivotal in accounting for multiple quantum phenomena[16-18], their role in mediating the formation of plasmons formation remains largely unclear and unexplored. Moreover, as correlated plasmons are intimately related to long-range charge correlations[10, 14], the detection of this quantum quasiparticle holds the potential to reveal valuable insights to the underlying mechanisms that result in its formation.

Rare earth perovskite-structure nickelates have garnered significant attention due to their unique electronic structures and rich phase diagram[19-21]. Among them, $LaNiO_3$ stands out with its metallic behavior and bifunctional catalytic activity[21-24]. Through the process of Sr-doping and other treatment techniques, the observation of charge density waves and the emergence of superconductivity in their reduced phases have raised further interest in this class of oxide system[25-28]. The investigation of plasmon dynamics is essential for gaining a deeper understanding of electronic correlations. Here, we present our observations and insights into the optical conductivity and unique paired energy correlated plasmons in $La_{1-x}Sr_xNO_3$ (LSNO) systems with varying doping concentration (x = 0 (LNO); x = 0.125 (LSNO(0.125)); x = 0.25 (LSNO(0.25))). We found that conventional metallic plasmons and correlated plasmons coexist in LNO, but the correlated plasmons disappear in LSNO(0.125). At higher Sr doping concentration in LSNO(0.25), the correlated plasmons re-emerge. Additionally, LSNO(0.125) exhibits significantly higher optical conductivity compared to LNO and LSNO(0.25). A series of spectroscopic ellipsometry (SE) and X-ray absorption spectroscopy (XAS) measurements substantiated demonstrate that the transitions between different plasmonic states and the anomalous optical conductivity (Fig. 1a) can be attributed to variations in the O2*p*-Ni3*d* orbital hybridization and effective interaction U^* (comprising the long-range Coulomb variable interactive components). These experimental results are further substantiated by first principles density functional theory (DFT) calculations. Analysis of of the effective interaction, U^*, suggests that the orbital hybridization effects may indirectly influence the long-range charge correlations in the LSNO system. Consequently, orbital hybridizations impact material plasmons excitation, regulate long-range electron correlation, and enhance optical conductivity fluctuation. These findings have promising implications for plasmonic-based device engineering research and our understanding of electronic correlations in strongly correlated systems.

2. Results and Discussion

2.1 Optical conductivity of LSNO epitaxial thin films

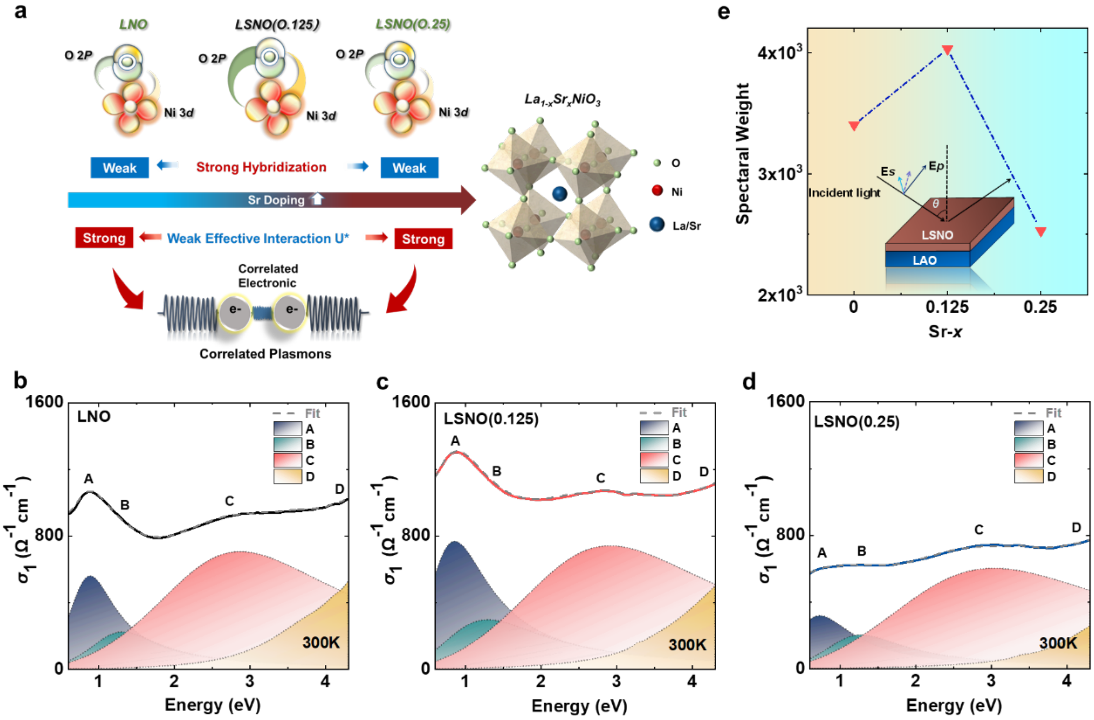

Fig. 1 (**a**) Illustration of the LSNO crystal structure and the underlying mechanism governing correlated plasmons. Real component of the optical conductivity, σ_1, of (**b**) LNO on LAO, (**c**) LSNO(0.125) on LAO, (**d**) LSNO(0.25) on LAO films at room temperature. Experimental spectra fitted by Drude-Lorentz peaks (shown as light-colored peak) and visual guides to identify positions of peaks A, B, C, and D in σ_1 spectra and the gray dotted line is the result of the fit. (**e**) The Spectral Weight obtained from (**b**), (**c**), and (**d**). Inset: Schematic illustration of spectroscopic ellipsometry experimental measurement.

20 u.c. LSNO thin films with different Sr doping levels (x = 0, 0.125, 0.25) were grown on (001)-oriented single crystal $LaAlO_3$ (LAO) substrates using oxygen plasma–assisted molecular beam epitaxy (OPA-MBE)[23]. All three samples demonstrate metallic behavior at room temperature, with the conductivity decreasing with increasing doping concentration, x. By analyzing the optical conductivity spectra, σ_1, (Fig. 1b-d), changes have been observed in their optical structures. To accurately analyze the optical features in each spectrum, RefFIT has been utilized where the

Drude-Lorentz model is employed to account for both the delocalized and localized charges in the respective systems[29]. The LSNO films at different doping concentrations exhibited generally similar optical characteristics, featuring distinct optical features labeled as A, B, C, and D (Figs. 1b-d). These optical features can be attributed to various inter-band transitions, as reported in previous studies[30, 31]. The σ_1 spectra combined with our calculations (see supplementary materials and Fig. 4a), feature A located at ~0.89 eV in the LNO film corresponds to the transition from Ni(t_{2g}) orbital to the Fermi surface while feature B (~1.32 eV) corresponds to transitions from Ni(t_{2g}) to the unoccupied Ni(e_g) orbital. The broad feature denoted C (~2.87 eV) is associated with transitions between the O2p and Ni(e_g) orbitals. Meanwhile feature D, with its centre located beyond the instrument measurement range, may be ascribed to the transition from the O2p orbital to antibonding Ni(e_g^A) orbital or the bonding Ni(e_g^B) orbital to Ni(e_g) orbital. The exact location of this optical feature is beyond our current measurements' capabilities. Similar analysis has also been performed for the other samples (see supplementary materials). These findings shed light on the evolving electronic structure in response to Sr doping, contributing to a deeper understanding of the optical properties of the materials under investigation.

The intensity of the σ_1 spectrum of LSNO(0.125) is stronger compared to other samples. This observation aligns with the findings in Fig. 1e, where the Spectral Weight (SW) appears to have increased in LSNO(0.125). Moreover, as demonstrated in Fig. S1, the feature peak positions of optical conductivity remain generally unchanged with temperature. This implies that, unlike other rare earth nickelates[32, 33], the correlation strength in the LSNO system is relatively insensitive to changes in temperature.

2.2 Conventional and Correlated Plasmons of LSNO epitaxial films

An analysis of the dielectric function, ε_1, is performed for each sample, along with their corresponding loss function (LF, where LF = $\mathrm{Im}(-1/\varepsilon(\omega)) = \varepsilon_2/(\varepsilon_1^2+\varepsilon_2^2)$) as displayed in Fig. 2. This set of analysis is essential to provide additional insights into the plasmonic behaviors of LSNO epitaxial films and how they evolve with varying doping concentration.

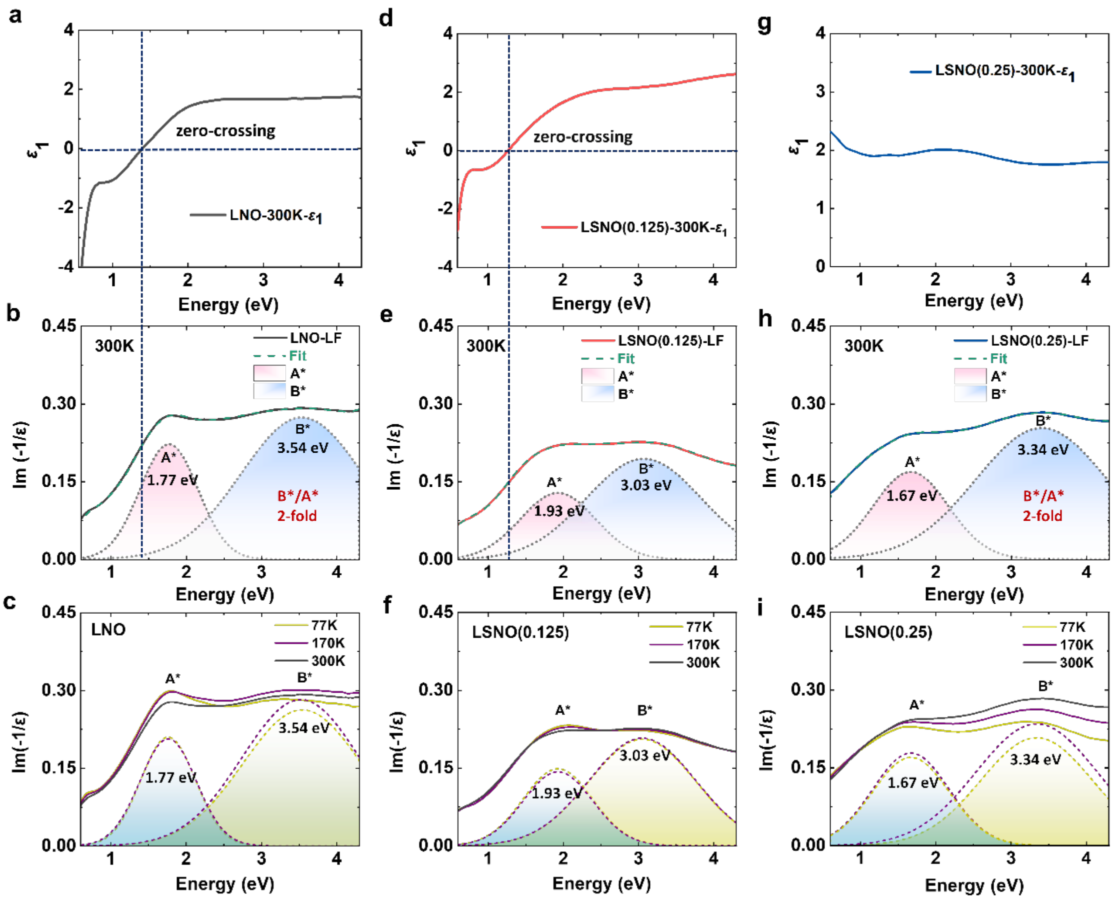

Fig. 2 (**a**, **d**, **g**) Real (ε_1) components of LNO/LAO films (**a**) and LSNO(0.125)/LAO films (**d**) and LSNO(0.25)/LAO films (**g**) at room temperature. (**b**, **e**, **h**) Loss-function spectra of LNO/LAO films (**b**) and LSNO(0.125)/LAO films (**e**) and LSNO(0.25)/LAO films (**h**) at room temperature. (**c**, **f**, **i**) Loss-function spectra of LNO/LAO films (**c**) and LSNO(0.125)/LAO films (**f**) and LSNO(0.25)/LAO films (**i**) at different temperature. Light dashed lines serve as visual guides in identifying positions of ε_1 zero-crossing and the green dotted line is the result of the fit. The color peaks are the fitting peaks, and the figures only shows the fitting results of peaks A* and B*.

Two distinct peaks labelled A* and B* have been observed in the LF spectra of the respective samples. These peaks are absent from their corresponding σ_1 and ε_1 spectra. As shown in Fig. 2a and 2b, peak A* (~1.77 eV) in the LF spectra of LNO is approximately in similar energy position with the zero-crossing of the corresponding ε_1 spectrum at ~1.39 eV. This alignment is a signature of conventional metallic plasmons, which are present in the metallic state of LNO[10, 12, 34]. In the case of LSNO(0.125), the metallic plasmons remain with peak A* (~1.93 eV) in the LF spectrum coinciding with the corresponding ε_1 zero-crossing at ~1.26 eV. The disparity in the positions of the ε_1 zero-crossing and the corresponding LF peaks can be attributed to the onset of free-electron scattering within the system[10]. For the LSNO(0.25) sample, the ε_1 spectrum no longer exhibits any zero-crossing and corresponding with the reduction of metallic properties.

In addition to peak A*, peak B* is also present in the LF spectra of the respective LSNO samples at a higher photon energy (Figs. 2b, e and h). Particularly for LNO and LSNO(0.25), there is a two-fold energy relationship between peaks A* and B*. However, such a two-fold energy relation between peaks A* and B* is absent from LSNO(0.125). Combining the optical features observed in the σ_1 spectra with peaks A* and B* in LF spectra, it becomes evident that these peaks do not originate from inter-band transitions, as seen in their σ_1 spectra. This suggests that, apart from the conventional metallic plasmon behavior represented by peak A* in the LF spectra of LSNO samples and the two-fold relationship between features A* and B*, there may be other plasmonic phenomena at play. Notably, similar experimental observations concerning correlated plasmons in Mott-like insulating oxides have been reported[8, 10]. These findings provide additional impetus for further investigation to the plasmonic behavior exhibited in LSNO samples.

To elucidate the two-fold relationship present in the LF spectra for both LSNO(0.25) and LNO, theoretical studies have suggested that the dispersion relation sufficiently changes and at the strong interaction strength[35], a pair of plasmonic peaks may arise in the LF spectrum, with one peak at energy U^* and another at quantization energy $\sim U^*/2$, where U^* denotes the effective interaction (U^* is formed of long-range interaction $V(\boldsymbol{q})$ and variable interaction U)[14]. The peak at U^* stems from collective excitations in the Mott correlated bands, while the peak at $U^*/2$ can be attributed to particle-hole excitations across Mott bands to the plasmon peak[14]. The observation of correlated plasmon has direct relevance in accounting for the presence of correlated plasmons that manifest themselves in the form peak A* and B* with two-fold relationship as evidenced in both LSNO(0.25) and LNO. Specifically, peak B* at ~3.54 eV in the LF spectra of LSNO(0.25) (Fig. 2h) is equivalent to U^* while Peak A*($U^*/2$) located half the energy of peak B* at ~1.77eV is the half-energy mode of the correlated plasmon associated with peak B*. This two-fold relationship between features A*(~1.67eV) and B*(~3.34 eV) is also present in LNO. This observation suggests the coexistence of both conventional metallic and correlated plasmons within the LNO system. Moreover, it is noteworthy that the presence of the correlated plasmons persists across the entire temperature range we measured in both LNO and LSNO(0.25), as evidenced by the presence of the 2-fold relationship between A* and B* in the LF spectra for both systems (Figs. 2c and 2i). It is essential to emphasize that the excitation of correlated plasmons exhibits significant variations as the temperature decreases, resulting in a notable reduction in plasmon peak intensity. In contrast, the excitation of conventional metallic plasmons remains largely unaffected by lowering the temperature. This disparity can be attributed to the unique behavior of correlated plasmons, which do not follow the conventional pattern associated with the zero-crossing of ε_1, as seen in the traditional metallic systems (absent in the case of correlated plasmons)[8, 10]. This phenomenon is particularly pronounced in LSNO(0.25), where the correlated plasmons originate from the oscillatory dynamics of localized correlated electrons rather than the free charges in conventional metallic systems. The contrast between the ε_1 spectra of LSNO(0.125) and LSNO(0.25) serves as a clear illustration of this distinction. The presence of correlated plasmons in LSNO adds to the complexity and richness of the electronic behavior in this intriguing material system.

The deviation of the two-fold relationship in LSNO(0.125) can be attributed to the effective interaction, U^*, having been weakened below a critical threshold energy known as U_c^*. Below this threshold, it is no longer favourable for the formation of correlated plasmons. Consequently, only a single broad plasmonic peak emerges,[14] as observed in LSNO(0.125), where plasmon peak B* broadens and redshifts to ~3.03 eV. The unique plasmon behavior in LSNO systems provides valuable insights into electronic correlations behaviors, which illustrate the reduction of the collective oscillations of the associated electrons in LSNO(0.125).

2.3 X-ray Absorption Spectra of LSNO epitaxial films

To gain further insights into how the electronic correlations and structure of the LSNO system evolve with Sr doping, detailed X-ray absorption spectroscopic (XAS) measurements are conducted on the respective samples. Figs. 3a and b display the Ni L_3-edges of the respective LSNO samples at both grazing (GI) and normal (NI) incidence. Besides the prominent La M_4-edge peak (~853.4eV) belonging to the La components in both the LSNO film and LAO substrate, the Ni L_3-edge feature appears in the form of feature *a*, along with a shoulder denoted as *a′*. These characteristics provide valuable information about the local Ni environment[36-40].

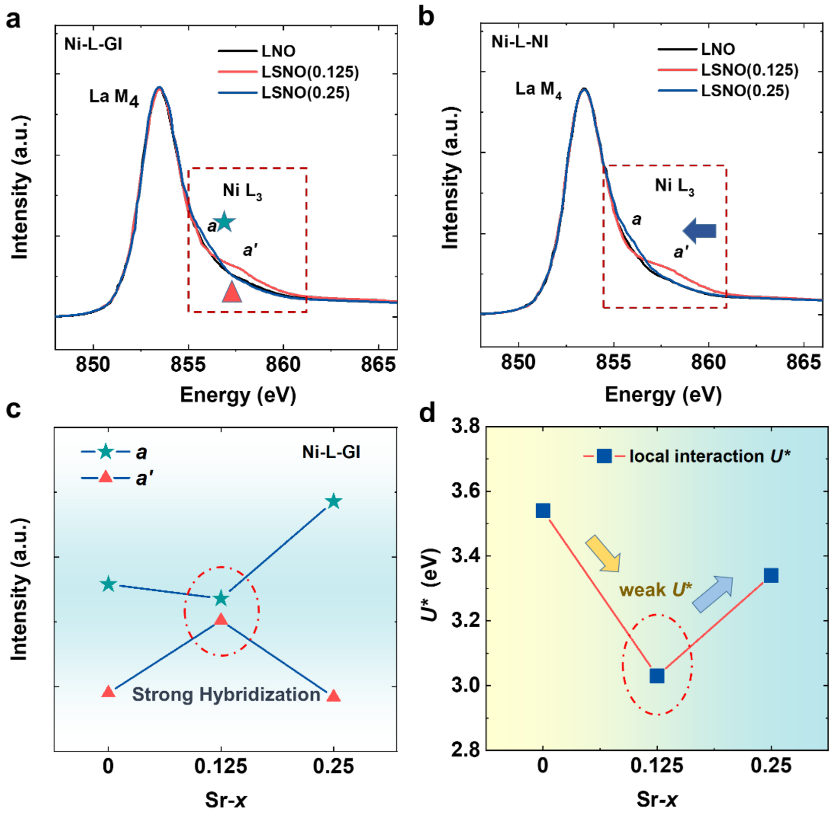

Fig. 3 (**a**) Grazing-incidence (GI) XAS and (**b**) normal-incidence (NI) XAS at the Ni L_3 edge for LNO/LAO films (black), LSNO(0.125)/LAO films (red) and LSNO(0.25)/LAO films (blue) at room temperature. (**c**) Voigt profile fitting conducted results for the intensity of respective Ni L_3-edge features *a* and *a'*. (**d**) Effective interaction *U** of LSNO(x=0,0.125,0.25)/LAO films with varying doping concentration. Red dotted circles serve as visual guides in identifying extreme value position of hybridization and effective interactions *U** with different Doping concentration in LSNO.

To examine the evolution of the intensity and position of features *a* and *a′* between LNO, LSNO(0.125) and LSNO(0.25), Voigt profile fitting is performed for the respective Ni L_3-edge features (see supplementary materials Fig. S3) with the results displayed in Fig. 3c. Across all three samples, the peak positions remain consistent. However, for LSNO(0.125), feature *a* has the lowest intensity while the intensity of feature *a'* maximises. To gain a deeper understanding of the orbital behavior, charge transfer multiplet calculations for Ni^{3+} in the D4*h*-symmetry were further conducted using CTM4XAS (Fig. S4)[41]. The outcomes of these calculations indicate that as the splitting parameter 10Dq increases, peak *a'* becomes more pronounced while peak *a* weakens. Previous theoretical calculations on LNO with a mixture of configurations $3d^7$, $3d^8\underline{L}$, $3d^9\underline{L}^2$ (where $\underline{L}$ denotes a ligand hole) in the ground state suggest that the variation in intensity of features *a* and *a'* is corresponds to changes in the Ni-O hybridization strength instead of changes to the Ni oxidation states[36, 39, 40]. Specifically, peak *a* arises due to the $2p^63d^7$—$2p^53d^8$ transition, while peak *a'* comes from the $2p^63d^8\underline{L}$—$2p^53d^9\underline{L}$ transition[41]. Meanwhile, previous theoretical and experimental studies have indicated that a higher intensity of feature *a'* than *a* indicates a stronger O2*p*-Ni3*d* hybridization strength. This suggests a direct correlation with an increased contribution of the $3d^8\underline{L}$ orbitals[37, 40]. Hence, it becomes evident that the intensity of the feature *a'* is closely tied to the strength of the O2*p*-Ni3*d* hybridization Where stronger hybridization leads to an increased intensity of feature *a*'. As shown in Fig. 3c, the intensity of feature *a'* which maximizes for LSNO(0.125) indicates that the O2*p*-Ni3*d* hybridization is strongest for the LSNO sample at this doping concentration, it is weakest for LSNO(0.25).

Furthermore, by comparing the effective interaction, U^*, (Fig. 3d) it can be concluded that U^* decreases with increasing doping concentration between LNO and LSNO(0.125). But as doping concentration continues to increase from LSNO(0.125) to LSNO(0.25), U^* rises again. Therefore, U^* is maximized for LSNO(0.125). The O2*p*-Ni3*d* orbital hybridization strength shows the same trend where it is maximized for LSNO(0.125) but is weakest for LSNO(0.25). Collectively, these trends suggest that orbital hybridization can indirectly influence the effective interaction strength, U^*. This, in turn, has the potential to modulate long-range interactions within the system, as U^* is a composite parameter that encompasses both long-range $V(\boldsymbol{q})$ and variable interactions.

2.4 DFT Calculates the Electronic Structure of LSNO Epitaxial Films

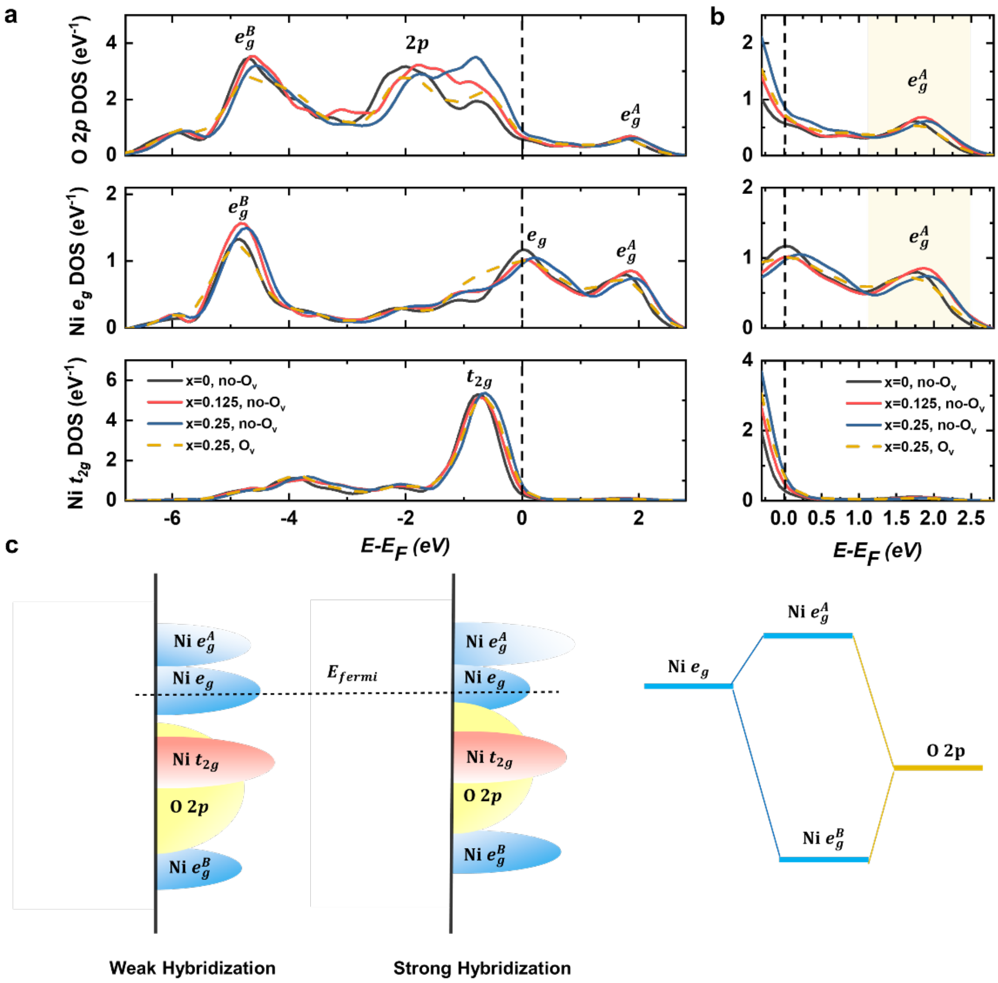

Fig. 4 (**a**) Density of states (DOS) of the respective constituent (Ni e_g, Ni t_{2g} and O 2*p*) orbitals for different doping concentration of x = 0, 0.125, 0.25 in LSNO. For x = 0.25, the presence of an oxygen vacancy case is considered, as depicted by the dashed line. (**b**) Enlarged view near the Fermi surface in Fig. 4a. (**c**) Schematic of the electronic structure in LSNO. Black dashed lines serve as visual guides in identifying positions of Fermi surface.

To further investigate how O2*p*–Ni3*d* orbital hybridization is dictated by Sr doping concentration, first principles calculations based on density functional theory (DFT) method has been implemented in Vienna atomic simulation package (VASP)[42-45]. Fig. 4a displays the density of states (DOS) projected in the O 2*p*, Ni e_g and Ni t_{2g} orbitals for the LSNO structures with Sr-doping of $x = 0$, $x = 0.125$, $x = 0.25$, respectively. Within the energy range from -5 to 2 eV, distinct peaks emerge in both the O 2p and Ni e_g states. These peaks can be attributed to the formation of bonding (e_g^B) and antibonding (e_g^A) states resulting from the hybridization of these two orbitals. Notably, there is another Ni e_g peak positioned at the Fermi level, however, it does not show substantial hybridization with O 2p orbitals, signifying its non-hybridized nature. The non-hybridized O 2p states can be found around -2 eV. The t_{2g} center is about -1 eV below the Fermi energy.

Furthermore, the DOS are observed to shift towards higher energies respect to the Fermi energy as the Sr doping concentration increases. This shift can be attributed to the decrease in occupied states resulting from the increase in hole doping. As a hole-doped system, further attention will be placed on the behavior of the hole carriers above the Fermi level[46, 47]. As shown in Fig. 4b, the most notable change observed with varying doping level (x) is the maximization of the DOS for hybridized states (e_g^A) of both Ni and O when x = 0.125, followed by a subsequent decrease thereafter. It is worth noting that the strength of feature e_g^A in LSNO(0.25) is lower than that in LNO, indicating a reversed trend when compared to the nonhybridized O 2p and Ni e_g states. The transfer of the DOS from the non-hybridized states to the hybridized states exhibits the enhancement of hybridization, thus reinforcing the agreement between our experimental findings and the calculated results. Remarkably, LSNO(0.125) exhibits the strongest O 2p–Ni 3d hybridization, followed by LNO, while LSNO(0.25) displays the weakest hybridization. Moreover, according to our DFT calculations, the formation energy of oxygen vacancies, Vo, decreases with increasing Sr doping concentration, making it easier for these Vo to form. Therefore, for the case of LSNO(0.25), we considered the influence of the oxygen vacancies and noticed that the O 2p–Ni 3d orbital hybridization significantly reduces after introducing Vo. This reduction arises from a significantly reduced population of O 2p orbitals available for hybridization with the Ni 3d orbitals (for more details, refer to the supplementary materials).

According to the calculation and experimental results, we also draw a schematic diagram of the electronic structure of LSNO as shown in Fig. 4c. From left to center panel, the hybridization between the O and the Ni states are enhanced, and the more states goes from the non-hybridized to the hybridized. In the language of the Ni electronic configuration, it goes from Ni $2p^7$ to $3d^8\underline{L}$or even $3d^9\underline{L}^2$, where $\underline{L}$ is the ligand hole.

The presence of correlated plasmons is particularly pronounce in LSNO(0.25) which registers the weakest Ni-O hybridization. This is followed by LNO. Conversely, the correlated plasmons vanish in LSNO(0.125) where Ni-O hybridization is the strongest. Meanwhile, the presence of conventional metallic plasmons follows an opposite trend where it vanishes in LSNO(0.25) where orbital hybridization is at its weakest. As discussed earlier, orbital hybridization and effective interactions, U^*, have strong influences on each other. Hence, we propose that the maximized Ni3*d*–O2*p* orbital hybridization, coupled with the diminishing U^* in LSNO(0.125) play a significant role in influencing correlated charge excitation. These accounts for the observed increase in optical conductivity and the absence of correlated plasmons in LSNO(0.125).

3. Conclusion

In summary, the evolution of conventional and correlated plasmons and the optical conductivity behavior in the LSNO spectra at different doping concentrations have been discussed and analyzed based on the experimental results elucidated from SE and XAS measurements. Specifically, we have observed the presence of correlated plasmons in both LNO and highly-doped LSNO(0.25), whereas the conventional plasmons, accompanied by an increase in optical conductivity, were observed in LSNO(0.125). Through a comprehensive analysis involving first-principles calculations and experimental spectra of LF spectra and XAS spectra, we have identified that the strength of the Ni-O orbital hybridization plays an important role in determining the effective interaction, U*, within the system. This, in turn, influences the formation and dissipation of correlated plasmons in the LSNO samples. This study provides valuable insights into how hybridization can be used to regulate correlated charge excitation and physical properties of the strongly correlated system. Furthermore, it prompts further exploration into whether orbital hybridization plays a role in nickel oxide superconductivity, opening new avenues for further investigations.

Method

Spectroscopic Ellipsometry Measurements.

We used spectroscopic ellipsometry (SE) with a photon energy of 0.60– 4.30 eV to measure the ellipsometry parameters Ψ (the ratio between the amplitude of p- and s-polarized reflected light) and Δ (the phase difference between of p- and s-polarized reflected light) with a 70° incident angle, which indicates that the spectra include both in-plane and out-of-plane contributions. The optical conductivity has been extracted from the parameters Ψ and Δ by utilizing an air/LSNO/LAO multilayer model (see details in Supporting Information), where the LSNO composed of an average homogeneous and uniform medium. The experiments are done at 77K, 170K and room temperature. Spectroscopic Ellipsometry has no charging issue due to its photon-in–photon-out methodology. Spectroscopic ellipsometry (SE) measurements are conducted using a custom-made Variable Angle Spectroscopic Ellipsometer (VASE) of J. A. Woollam Co. Inc..

X-ray Absorption Spectroscopy Measurements. X-ray Absorption Spectroscopy (XAS) measurements were carried out on LSNO/LAO films at the Soft X-ray–Ultraviolet (SUV) beamline at the Singapore Synchrotron Light Source in a vacuum chamber with a base pressure of ~1×10^{-9} mbar via the Total Electron Yield (TEY) mode. The incident X-ray was directed at the sample surfaces at a normal incident angle and grazing-incidence. All experiments were conducted at room temperature.

The first-principles calculations. We did the first principles calculations with the density functional theory method implemented in Vienna atomic simulation package (VASP)[42-45]. The plane wave basis set with energy cutoff of 520 eV is used. The pseudopotential within the projected augmented wave (PAW) method is used[48]. We use the MonkHorst-Pack mesh of $n \times n \times n$ where n is about $30/l$, where is the l is the length of the cell parameter in Angstrom. We use the PBEsol density functional, which is optimized for computing the lattice structure in solid. In $La_{1-x}Sr_xNiO_3$ structure, no magnetic order is observed, so we use non-spin-polarized calculation. The $R\overline{3}c$ phase of the $LaNiO_3$ is assumed to be across all the Sr doping levels.

Data availability

The data that support the findings of this study are available within the article and its Supplementary Information. Additional relevant data are available from the corresponding authors upon reasonable request.

Acknowledgements

This work was supported in part by the Strategic Priority Research Program of the Chinese Academy of Sciences, Grant No. XDB25000000, National Natural Science Foundation (52172271), the National Key R&D Program of China No. 2022YFE03150200, Shanghai Science and Technology Innovation Program (22511100200). Work at PNNL were supported by the U.S. Department of Energy (DOE), Office of Science, Basic Energy Sciences, Division of Materials Sciences and Engineering, Synthesis and Processing Science Program, under Award #10122. C.S.T. acknowledges the support from the NUS Emerging Scientist Fellowship. The authors would like to acknowledge the Singapore Synchrotron Light Source for providing the facility necessary for conducting the research. The Laboratory is a National Research Infrastructure under the National Research Foundation, Singapore. Any opinions, findings, and conclusions or recommendations expressed in this material are those of the author(s) and do not reflect the views of National Research Foundation, Singapore. [X. H acknowledges financial support from F.R.S.-FNRS through the PDR Grants PROMOSPAN (T.0107.20)]

Author contributions

X.Y. conceived the project. L.J., Y.D., and L.W. synthesized the samples. L.W. performed the electron transport experiments. C.S.T. performed the XRD and XAS experiments and M.S analyzed the data. M.S., C.S.T., X.L., M.C., D.L. performed the SE experiments and analyzed the data. X. H. performed the DFT analysis. M.S., C.S.T., X.H., L.W., and X.Y. wrote the manuscript, with input from all the authors.

Competing interests

The authors declare no competing interests.

Correspondence and requests for materials should be addressed to Chi Sin Tang or Le Wang or Xinmao Yin.

References

1. Inoue, J. & Maekawa, S. Spiral State and Giant Magnetoresistance in Perovskite Mn Oxides. *Phys. Rev. Lett*. **74**, 3407-3410 (1995).
2. Tokura, Y., Kawasaki, M. & Nagaosa, N. Emergent functions of quantum materials. *Nat. Phys*. **13**, 1056-1068 (2017).
3. Balents, L., Dean, C.R., Efetov, D.K. & Young, A.F. Superconductivity and strong correlations in moiré flat bands. *Nat. Phys*. **16**, 725-733 (2020).
4. Rau, J.G., Lee, E.K.-H. & Kee, H.-Y. Spin-Orbit Physics Giving Rise to Novel Phases in Correlated Systems: Iridates and Related Materials. *Annu. Rev. Condens. Matter Phys*. **7**, 195-221 (2016).
5. Shi, J., Zhou, Y. & Ramanathan, S. Colossal resistance switching and band gap modulation in a perovskite nickelate by electron doping. *Nat. Commun.* **5**, 4860 (2014).
6. Miller, T.A. et al. Terahertz field control of in-plane orbital order in La(0.5)Sr(1.5)MnO4. *Nat. Commun* **6**, 8175 (2015).
7. Yadav, A.K. et al. Observation of polar vortices in oxide superlattices. *Nature* **530**, 198-201 (2016).
8. Asmara, T.C. et al. Tunable and low-loss correlated plasmons in Mott-like insulating oxides. *Nat. Commun* **8**, 15271 (2017).
9. Khandelwal, A., Mohammad Tashrif, S. & Rusydi, A. Coupled harmonic oscillator models for correlated plasmons in one-dimensional and quasi-one-dimensional systems. *J. Phys.: Condens. Matter*. **34** (2021).
10. Yin, X. et al. Quantum Correlated Plasmons and Their Tunability in Undoped and Doped Mott-Insulator Cuprates. *ACS Photonics* **6**, 3281-3289 (2019).
11. Vast, N., Reining, L., Olevano, V., Schattschneider, P. & Jouffrey, B. Local field effects in the electron energy loss spectra of rutile TiO2. *Phys. Rev. Lett*. **88**, 037601 (2002).
12. Tang, C.S. et al. Interfacial Oxygen-Driven Charge Localization and Plasmon Excitation in Unconventional Superconductors. *Adv. Mater* **32**, e2000153 (2020).
13. Zhu, T. et al. Generation of multiple plasmons in strontium niobates mediated by local field effects. *Phys. Rev. B*. **98**, 235115 (2018).
14. van Loon, E.G., Hafermann, H., Lichtenstein, A.I., Rubtsov, A.N. & Katsnelson, M.I. Plasmons in strongly correlated systems: spectral weight transfer and renormalized dispersion. *Phys. Rev. Lett.* **113**, 246407 (2014).
15. Whitcher, T.J. et al. Correlated plasmons in the topological insulator Bi2Se3 induced by long-range electron correlations. *NPG Asia Materials* **12**, 37 (2020).
16. Middey, S. et al. Polarity compensation in ultra-thin films of complex oxides: the case of a perovskite nickelate. *Sci. Rep.* **4**, 6819 (2014).
17. Hidaka, M. et al. Metal–insulator transition induced by electronic and structural modulations in oxygen-deficient perovskite-type TbBaCo2O5.5. *Phys. Rev. B*. **243**, 1813-1822 (2006).
18. Nakao, H. et al. Charge disproportionation of Mn 3d and O 2p electronic states depending

on strength of p−d hybridization in (LaMnO3)2(SrMnO3)2 superlattices. *Phys. Rev. B.* **98**, 245146-245146 (2018).

19. Catalano, S. et al. Rare-earth nickelates RNiO(3): thin films and heterostructures. *Rep Prog Phys* **81**, 046501 (2018).
20. Wang, L. et al. Spontaneous phase segregation of Sr2NiO3 and SrNi2O3 during SrNiO3 heteroepitaxy. *Sci. Adv.* **7**, 2866 (2021).
21. Suntivich, J., May, K.J., Gasteiger, H.A., Goodenough, J.B. & Shao-Horn, Y. A Perovskite Oxide Optimized for Oxygen Evolution Catalysis from Molecular Orbital Principles. *Science* **334**, 1383-1385 (2011).
22. Petrie, J.R. et al. Enhanced Bifunctional Oxygen Catalysis in Strained LaNiO3 Perovskites. *J. Am. Chem. Soc.* **138**, 2488-2491 (2016).
23. Liu, J. et al. Tuning the Electronic Structure of LaNiO3 through Alloying with Strontium to Enhance Oxygen Evolution Activity. *Adv. Sci.* **6**, 1901073 (2019).
24. Wang, L. et al. T uning Bifunctional Oxygen Electrocatalysts by Changing the A-Site Rare-Earth Element in Perovskite Nickelates. *Adv. Funct. Mater* **28**, 1803712 (2018).
25. Osada, M. et al. Nickelate Superconductivity without Rare-Earth Magnetism: (La,Sr)NiO2. *Adv. Mater.* **33**, 7 (2021).
26. Lin, J.Q. et al. Strong Superexchange in a d;9-delta Nickelate Revealed by Resonant Inelastic X-Ray Scattering. *Phys. Rev. Lett.* **126**, 087001 (2021).
27. Zhang, J. et al. Intertwined density waves in a metallic nickelate. *Nat. Commun* **11**, 6003 (2020).
28. Kang, C.-J. & Kotliar, G. Optical Properties of the Infinite-Layer La1−xSrxNiO2 and Hidden Hund's Physics. *Phys. Rev. Lett.* **126**, 127401 (2021).
29. Kuzmenko, A.B. Kramers–Kronig constrained variational analysis of optical spectra. *Sci. Instrum.* **76**, 83108-83108 (2005).
30. Stewart, M.K. et al. Optical probe of strong correlations in LaNiO3 thin films. *J. Appl. Phys*. **110**, 1915 (2011).
31. Stewart, M.K. et al. Optical study of strained ultrathin films of strongly correlated LaNiO3. *Phy. Rev. B*. **83**, 075125 (2011).
32. Ruppen, J. et al. Optical spectroscopy and the nature of the insulating state of rare-earth nickelates. *Phy. Rev. B*. **92**, 155145 (2015).
33. Katsufuji, T., Okimoto, Y., Arima, T., Tokura, Y. & Torrance, J.B. Optical spectroscopy of the metal-insulator transition in NdNiO3. *Phy. Rev. B*. **51**, 4830-4835 (1995).
34. Pines, D. Collective Energy Losses in Solids. *Reviews of Modern Physics* **28**, 184-198 (1956).
35. Maksim Ulybyshev, C.W., and Savvas Zafeiropoulos Collective charge excitations and the metal-insulator transition in the square lattice Hubbard-Coulomb model. *Phy. Rev. B*. **96**, 205115 (2017).
36. Kumar, Y. et al. Irradiation induced modification in transport properties of LaNiO3 thin films: An x-ray absorption study. *Applied Physics Letters* **101**, 8209 (2012).
37. Kumar, Y. et al. Ni 3d – O 2p hybridization dependent magnetic properties of LaNiO3 thin films. *Thin Solid Films* **619**, 144-147 (2016).
38. Grisolia, M.N. et al. Hybridization-controlled charge transfer and induced magnetism at correlated oxide interfaces. *Nat. Phys.* **12**, 484-492 (2016).

39. Fujimori., T.M.a.A., Tokura., T.A.a.Y., Mori., N. & Akimitsu., J. Electronic structure of PrNi03 studied by photoemission and x-ray-absorption spectroscopy:Band gap and orbital ordering. *Phy. Rev. B*. **52**, 13865-13873 (1995).
40. Piamonteze, C. et al. Spin-orbit-induced mixed-spin ground state inRNiO3perovskites probed by x-ray absorption spectroscopy: Insight into the metal-to-insulator transition. *Phy. Rev. B*. **71**, 020406 (2005).
41. Stavitski, E. & de Groot, F.M. The CTM4XAS program for EELS and XAS spectral shape analysis of transition metal L edges. *Micron* **41**, 687-694 (2010).
42. Furthmiiller, G.K.a.J. Efficiency of ab-initio total energy calculations for metals and semiconductors using a plane-wave basis set. *Computational Materials Science* **6**, 15-50 (1996).
43. Furthmu¨ller, G.K.a. Efficient iterative schemes for ab initio total-energy calculations using a plane-wave basis set. *Phy. Rev. B*. **54**, 11169-11186 (1996).
44. Hafner, G.K.a.J. Ab initio molecular dynamics for liquid metals. *Phy. Rev. B*. **47**, 558-561 (1993).
45. Hafner, G.K.a.J. Ab initio molecular-dynamics simulation of the liquid-metal — amorphous-semiconductor transition in germanium. *Phy. Rev. B*. **49**, 14251-14269 (1994).
46. Huanjun Ding, K.P., Yongli Gao Evolution of the unoccupied states in alkali metal-doped organic semiconductor. *J. Electron Spectrosc. Relat. Phenom.* **174**, 45-49 (2009).
47. Stefanie Winkler, P.A., Johannes Frisch, Martin Oehzelt, Georg Heimel and Norbert Koch Probing the energy levels in hole-doped molecular semiconductors. *Materials Horizons* **2**, 427- 433 (2015).
48. Joubert, G.K.a.D. From ultrasoft pseudopotentials to the projector augmented-wave method. *Phy. Rev. B*. **59**, 1758-1775 (1999).